The Astronomical Journal, 157:148 (14pp), 2019 April https://doi.org/10.3847/1538-3881/ab0956

The Blueshift of the C IV Broad Emission Line in QSOs

Xue Ge[1], Bi-Xuan Zhao[1], Wei-Hao Bian[1], and Green Richard Frederick[2]
[1] School of Physics and Technology, Nanjing Normal University, Nanjing 210023, People's Republic of China; whbian@njnu.edu.cn
[2] Steward Observatory, University of Arizona, Tucson, AZ 85721, USA
Received 2018 November 28; revised 2019 February 2; accepted 2019 February 19; published 2019 March 20

Abstract

For the sample from Ge et al. of 87 low-z Palomar–Green quasi-stellar objects (QSOs) and 130 high-z QSOs ($0 < z < 5$) with Hβ-based single-epoch supermassive black hole masses, we perform a uniform decomposition of the C IV λ1549 broad-line profile. Based on the rest frame defined by the [O III] λ5007 narrow emission line, a medium-strong positive correlation is found between the C IV blueshift and the luminosity at 5100 Å or the Eddington ratio $L_{\rm Bol}/L_{\rm Edd}$. A medium-strong negative relationship is found between the C IV blueshift and C IV equivalent width. These results support the postulation where the radiation pressure may be the driver of C IV blueshift. There is a medium-strong correlation between the mass ratio of C IV-based to Hβ-based $M_{\rm BH}$ and the C IV blueshift, which indicates that the bias for C IV-based $M_{\rm BH}$ is affected by the C IV profile.

Key words: black hole physics – galaxies: active – quasars: emission lines

1. Introduction

Broad emission lines are the most prominent spectral features of Type I active galactic nuclei (AGNs) and quasi-stellar objects (QSOs). It is believed that broad emission lines are produced by photoionization. The ionizing photons are from the accretion disk surrounding the central supermassive black hole (SMBH) in AGNs/QSOs. These photons irradiate the high-velocity clouds in broad-line regions (BLRs) and the subsequent recombination produces the broad emission lines. The broad emission lines have been studied for many years with regard to their geometry and kinematics. The observed properties of broad emission lines including the width, strength, and profile can give us insight into the physical processes in the central regions of AGNs/QSOs (e.g., Wang et al. 2017).

The blueshift of the C IV emission line relative to low-ionization lines is unambiguously detected in many samples (e.g., Gaskell 1982; Vanden Berk et al. 2001; Richards et al. 2002; Wang et al. 2011). It indicates that an outflowing wind may be a common configuration for the BLR clouds (Gaskell 1982; Marziani et al. 1996; Leighly 2004). Richards et al. (2011) proposed a two-component model for BLRs, namely a wind and a disk component. In this model, a stronger extreme-ultraviolet (EUV) ionizing continuum will reduce the wind component relative to the disk lines by ionizing the atoms that would otherwise produce the line-driven wind; for weaker EUV/soft X-ray, the wind component can develop, and the disk component is further reduced because the wind absorbs some of the ionizing continuum. The C IV blueshift quantifies the relative strength of these two components. The C IV equivalent width (EW) quantifies the total BLR gas and ionizing UV photons reaching the disk.

Actually, the accuracy of the C IV blueshift determination depends on the measurement of systemic redshift. There are several ways used to obtain AGNs/QSOs redshifts: (1) host galaxy absorption lines. However, these host absorption lines are usually contaminated by the light from the AGN/QSOs in spatially unresolved spectra. It makes the absorption lines too weak to be recognized. (2) The narrow [O III] or Balmer lines: these lines have been measured to have very low blueshifts or redshifts (e.g., Marziani et al. 1996; Sulentic et al. 2000; Richards et al. 2002; Hewett & Wild 2010). In more distant QSOs ($z > 0.8$), [O III] and Hβ have shifted into the near-infrared (NIR), for which infrared spectrographs need be used to measure the common rest-frame optical lines of these QSOs. (3) UV emission lines: Mg II λ2798 is accepted to be the most dependable UV emission line for the measurement of AGNs/QSOs redshifts (e.g., Tytler & Fan 1992). However, when $z > 2.2$, the wavelength of Mg II moves beyond the optical window. C IV λ1549 will be a reliable alternative for the measurement of redshift when Mg II is not available. However, the C IV outflow makes measurements of the redshifts difficult.

The Hβ line is widely adopted to estimate the $M_{\rm BH}$ of AGNs/QSOs (e.g., Kaspi et al. 2000; McLure & Jarvis 2002; Collin et al. 2006; Vestergaard & Peterson 2006; Onken & Kollmeier 2008; Ge et al. 2016) because of its calibration through reverberation mapping at low redshift. For the high-ionization lines, such as C IV, Baskin & Laor (2004b) found that for QSOs with Hβ FWHM < 4000 km s^{-1}, the C IV-based $M_{\rm BH}$ is higher by a factor of 3–4 than the Hβ-based $M_{\rm BH}$. In contrast, for QSOs with Hβ FWHM > 4000 km s^{-1}, the C IV-based $M_{\rm BH}$ is lower by the same factor. The C IV-based $M_{\rm BH}$ is biased with respect to the Hβ-based $M_{\rm BH}$ (e.g., Bian et al. 2012; Shen & Liu 2012). The uncertainties in the determination of $M_{\rm BH}$ may arise from the non-virial component shown in the line profile, such as from a radiation-driven disk wind (e.g., Murray et al. 1995; Proga et al. 2000; Richards et al. 2011; Coatman et al. 2017).

In this paper, for a compiled sample of low-z Palomar–Green (PG) QSOs and high-z QSOs, spectral decomposition is used to investigate the blueshift of the C IV broad emission line relative to [O III] λ5007. The sample and analysis are described in Section 2. Our result and a discussion are given in Section 3. Finally, our conclusions are presented in Section 4. All of the cosmological calculations in this paper assume $H_0 = 70$ km s^{-1} Mpc^{-1}, $\Omega_M = 0.3$, and $\Omega_\Lambda = 0.7$.

2. Sample and Analysis

2.1. Sample Selection

A low-z sample is adopted from the optically selected sample of PG QSOs (Boroson & Green 1992). It contains 87 PG QSOs with $0 < z < 0.5$ from the Bright Quasar Survey (Schmidt & Green 1983). It is the most thoroughly explored sample of

Table 1
A Summary of PG QSOs

#	Name	z	Velocity Shift (km s^{-1})	Error of Velocity Shift (km s^{-1})	$L^{\dagger}_{5100}$ (erg s^{-1})	$M^{\dagger}_{\rm BH}$ $M_{\odot}$	$L_{\rm bol}/L^{\dagger}_{\rm Edd}$
(1)	(2)	(3)	(4)	(5)	(6)	(7)	(8)
1	0003+158*	0.450	0	19	46.02	9.273	−0.388
2	0003+199*	0.025	−194	19	43.72	7.152	−0.566
3	0007+106	0.089	−194	39	44.73	8.689	−1.089
4	0026+129*	0.142	−968	19	44.91	8.594	−0.818
5	0049+171	0.064	−387	232	43.81	8.254	−1.575
6	0050+124*	0.061	1356	39	44.71	7.402	0.173
7	0052+251*	0.155	775	39	44.75	8.567	−0.951
8	0157+001	0.164	1937	39	44.91	8.137	−0.360
9	0804+761	0.100	0	58	44.85	8.841	−1.125
10	0838+770	0.131	−387	174	44.63	8.110	−0.610
11	0844+349	0.064	−194	97	44.37	7.966	−0.733
12	0921+525	0.035	−581	39	43.59	7.400	−0.944
13	0923+129	0.190	−387	58	43.65	8.495	−1.982
14	0923+201	0.029	−968	136	44.98	7.984	−0.136
15	0947+396*	0.206	194	39	44.73	8.638	−1.047
16	0953+414*	0.239	1356	39	45.13	8.441	−0.445
17	1011−040	0.058	0	77	44.10	7.243	−0.272
18	1012+008	0.185	968	116	44.95	8.220	−0.403
19	1022+519	0.045	0	116	43.46	7.028	−0.706
20	1048−090	0.344	−968	426	45.60	9.206	−0.744
21	1048+342	0.167	581	329	44.61	8.324	−0.845
22	1049−005*	0.357	0	19	45.63	9.183	−0.684
23	1100+772*	0.313	387	39	45.58	9.275	−0.834
24	1103−006*	0.425	0	97	45.67	9.326	−0.793
25	1115+407*	0.154	581	77	44.51	7.616	−0.237
26	1116+215*	0.177	968	39	45.38	8.523	−0.279
27	1119+120	0.049	0	97	43.96	7.387	−0.561
28	1121+422*	0.234	2518	19	44.81	7.996	−0.322
29	1149−110	0.049	581	77	43.93	7.839	−1.042
30	1151+117	0.176	0	58	44.67	8.507	−0.975
31	1202+281*	0.165	775	19	44.49	8.560	−1.202
32	1211+143	0.085	−194	39	45.02	7.938	−0.053
33	1216+069*	0.334	387	19	45.72	9.199	−0.612
34	1226+023*	0.158	581	39	45.90	8.947	−0.181
35	1229+204	0.064	387	39	43.64	7.865	−1.359
36	1259+593*	0.472	1937	252	45.91	8.920	−0.148
37	1302−102*	0.286	1937	39	45.83	8.882	−0.189
38	1307+085*	0.155	−194	39	44.79	8.643	−0.987
39	1310−108	0.035	−194	58	43.49	7.769	−1.413
40	1322+659*	0.168	581	19	44.92	8.252	−0.469
41	1341+258	0.087	−387	194	44.20	7.969	−0.901
42	1352+183*	0.158	2324	58	44.73	8.385	−0.785
43	1402+261*	0.164	581	77	44.92	7.915	−0.129
44	1415+451*	0.114	581	39	44.45	7.961	−0.647
45	1416−129*	0.129	0	58	45.09	9.025	−1.070
46	1425+267*	0.366	1549	174	45.76	9.737	−1.110
47	1426+015	0.086	0	97	44.57	9.113	−1.677
48	1427+480*	0.221	0	19	44.67	8.046	−0.510
49	1435−067	0.129	194	58	44.85	8.332	−0.619
50	1440+356*	0.077	581	39	44.43	7.413	−0.117
51	1444+407*	0.267	775	155	45.16	8.273	−0.242
52	1501+106	0.036	194	58	44.13	8.451	−1.450
53	1512+370*	0.371	194	39	45.60	9.376	−0.908
54	1519+226	0.137	775	77	44.62	7.897	−0.416
55	1534+580	0.030	−194	39	43.45	8.085	−1.774
56	1543+489*	0.400	2130	58	45.43	7.995	0.303
57	1545+210*	0.266	194	58	45.41	9.309	−1.030
58	1612+261*	0.131	−387	39	44.62	8.014	−0.525
59	1613+658	0.129	581	77	44.71	8.446	−0.870
60	1617+175	0.114	387	155	44.33	8.774	−1.578
61	1626+554*	0.133	581	58	44.47	8.446	−1.111
62	2130+099	0.061	−581	39	44.14	8.660	−1.654

Table 1
(Continued)

#	Name	z	Velocity Shift (km s^{-1})	Error of Velocity Shift (km s^{-1})	$L^{\dagger}_{5100}$ (erg s^{-1})	$M^{\dagger}_{\rm BH}$ $M_{\odot}$	$L_{\rm bol}/L^{\dagger}_{\rm Edd}$
(1)	(2)	(3)	(4)	(5)	(6)	(7)	(8)
63	2209+184	0.070	775	174	44.34	8.706	−1.496
64	2214+139	0.067	0	97	44.56	8.503	−1.076
65	2251+113*	0.323	−387	39	45.69	8.992	−0.433
66	2304+042	0.042	0	58	43.88	8.476	−1.726
67	2308+098*	0.432	−194	39	45.78	9.595	−0.952

Note. Column (1): sequence number; column (2): name of PG QSOs, ∗ in column (2) indicate the observations that are from *HST*; column (3): redshift from Schmidt & Green (1983); columns (4) and (5): shift of C IV peak wavelength and the error, positive value means blueshift; column (6): luminosity of 5100 Å; columns (7) and (8): the host-corrected $M_{\rm BH}$ and Eddington ratio (in logarithm scale). † means that the data is from Ge et al. (2016).

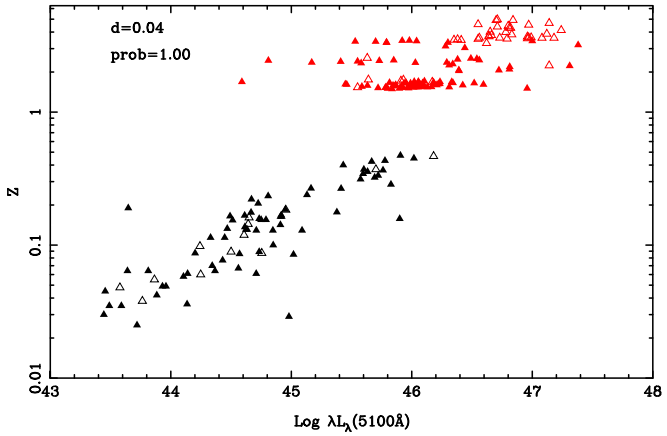

Figure 1. Distribution of low-z QSOs (black) and high-z QSOs (red) in z-λL_{λ}(5100Å) space.The hollow triangles are excluded from our sample. The labels in the panel are the two-dimension K–S test.

AGN/QSO, with a lot of high-quality broadband data, including X-ray, optical, infrared, and radio (e.g., Boroson & Green 1992; Brandt et al. 2000; Baskin & Laor 2004a, 2004b; Shi et al. 2014; Bian et al. 2016). The optical spectra of the 87 objects are from the Gold Spectrograph on the Kitt Peak National Observatory (KPNO) 2.1 m telescope. The resolution of the spectra is 6.5 Å corresponding to ∼400 km s^{-1}. The redshift of each QSO was measured from the [O III] λ 5007 narrow emission line except for eight QSOs with weak or absent [O III]. Their redshifts were measured through the Hβ line (Boroson & Green 1992).

The UV spectra covering C IV 1549Å of 85 PG QSOs are available in the MAST archive, 47 from the *Hubble Space Telescope* (*HST*), and 38 from the *International Ultraviolet Explorer* (*IUE*). Three sources, PG 0934+013, PG 1004+130, and PG 1448+273, do not have enough signal-to-noise ratio (S/N) to fit their C IV profiles. We also exclude 15 sources that are heavily absorbed in the C IV region (Laor & Brandt 2002; Baskin & Laor 2004b) because our fitting method used here is not suitable for profiles with a broad absorption line (BAL). Finally, there are 67 PG QSOs which are available for spectral decomposition. The UV spectra for 35 PG QSOs are available from *HST*, which were observed with the Faint Object Spectrograph (FOS) covering the wavelength range of 1150–8500 Å. The spectral resolutions ($R = \lambda/\Delta\lambda$) for FOS observations are $R \approx 1300$ and $R \approx 250$ at high and low spectral resolution, respectively. The UV spectra for the 32 PG QSOs are available from *IUE* with a spectral resolution of $R \approx 200$ (Anand et al. 2009). The wavelength range of the *IUE* UV spectra are 1151–2000 Å and 1850–3400 Å at short-wavelength prime (SWP) and long-wavelength prime (LWP), respectively. For some PG QSOs with *IUE* spectra, we did not add other observations, although a small number of sources were observed again using other spectrographs. We think that the choice of spectrographs of will not impact our results. Table 1 lists the information for these 67 PG QSOs.

The Sloan Digital Sky Survey (SDSS) I/II data (data release from 1 to 7, DR1-DR7) are available from the dedicated wide-field 2.5 m telescope (Gunn et al. 2006) at Apache Point Observatory near Sacramento Peak in southern New Mexico. The spectral resolution is up to 69 km s^{-1}. The wavelength range is from 3800 Å to 9200 Å. SDSS III (data release from 8 to 12, DR8-DR12) extends the range of wavelength from 3600 Å to 10400 Å. Ge et al. (2016) collected 181 high-z QSOs with Hβ-based $M_{\rm BH}$ from different literatures. They cross-matched the high-z sources with Shen et al. (2011) and obtained only 125 sources with C IV fitting data.[3] In this paper, we use 130 out of 181 sources where 125 objects are from Ge et al. (2016) and their UV spectra are obtained from SDSS DR7 (Abazajian et al. 2009; York et al. 2000). For 5 of the 130 high-z QSOs (i.e., TON618, UM667, SDSSJ105123+35453, SDSSJ153650+50081, and SDSSJ165354+40540), their UV spectra are from SDSS DR12 (Pâris et al. 2016) because the UV spectra with C IV are not available in SDSS DR7.

To get reliable measurements of the blueshift of the C IV line, we constructed a subsample from these low-z and high-z QSOs, i.e., 67 PG QSOs and 112 high-z QSOs. For high-z QSOs, we eliminated nine BAL QSOs identified by Shen et al. (2011) and visualizing, and seven weak-line sources from Shemmer & Lieber (2015). In addition, we also excluded Q0142-100 and PG 1115+080 from Assef et al. (2011), because of the lack of a redshift estimate from [O III] or Hβ/Hα. The high-z QSOs in the subsample comprise 112 QSOs, where 60 are from Shen & Liu (2012), 3 are from Assef et al. (2011), 12 are from Shemmer et al. (2004), 15 are from Netzer et al. (2007), and 22 are from Jun et al. (2015). We perform the two-dimensional Kolmogorov–Smirnov (K–S) test on the entire sample and subsample and find no significant difference between the two samples (Figure 1). The large p value (>0.001) shows that our selection of subsample does not significantly affect the results of this work. We call the subsample as "sample," which will be analyzed in following sections. Table 2 lists the information for these high-z QSOs.

[3] SDSS081331+254503 and HS0810+2554 in their Table 2 are actually the same.

Table 2
A Summary of High-z QSOs

#	Name	$z_{\rm fit}$	Velocity Shift (km s^{-1})	Error of Velocity Shift (km s^{-1})	$L^{\dagger}_{5100}$ (erg s^{-1})	$M^{\dagger}_{\rm BH}$ $M_{\odot}$	$L_{\rm bol}/L^{\dagger}_{\rm Edd}$	Reference
(1)	(2)	(3)	(4)	(5)	(6)	(7)	(8)	(9)
1	SDSS225800.02−084143	1.496	793	80	45.836	8.835	−0.129	a
2	SDSS035856.73−054023	1.506	649	133	45.800	9.065	−0.395	a
3	SDSS133321.90+005824	1.511	−152	30	45.897	9.391	−0.624	a
4	SDSS081331.28+254503	1.513	14	19	46.957	9.802	0.025	a
5	SDSS152111.86+470539	1.517	71	25	45.973	9.312	−0.469	a
6	FBQ1633+3134	1.522	519	185	45.720	9.096	−0.506	b
7	SDSS085543.26+002908	1.525	303	30	45.781	9.284	−0.633	a
8	SDSS123355.21+031327	1.528	904	71	45.927	9.591	−0.794	a
9	SDSS104910.31+143227	1.540	776	29	46.013	9.036	−0.153	a
10	SDSS154212.90+111226	1.540	1500	106	46.055	9.498	−0.573	a
11	SDSS143230.57+012435	1.542	1764	67	45.966	8.755	0.081	a
12	SDSS074029.82+281458	1.545	1263	36	46.041	9.514	−0.603	a
13	SDSS081344.15+152221	1.545	1391	75	46.031	9.391	−0.490	a
14	SDSS082146.22+571226	1.546	1225	49	46.311	9.429	−0.248	a
15	SDSS171030.20+602347	1.549	−443	54	46.129	9.655	−0.656	a
16	SDSS123442.16+052126	1.550	985	52	46.163	9.816	−0.783	a
17	SDSS015733.87−004824	1.551	497	162	45.786	9.352	−0.696	a
18	SDSS101447.54+521320	1.552	396	54	46.016	9.015	−0.129	a
19	SDSS135439.70+301649	1.553	600	45	46.097	9.465	−0.498	a
20	SDSS223246.80+134702	1.557	−254	34	46.060	9.762	−0.832	a
21	SDSS100930.51+023052	1.557	42	52	45.586	9.051	−0.595	a
22	SDSS124006.70+474003	1.561	644	40	45.978	8.864	−0.016	a
23	SDSS093318.49+141340	1.561	246	53	46.099	9.649	−0.680	a
24	SDSS094126.49+044328	1.567	394	44	45.854	9.455	−0.731	a
25	SDSS113829.33+040101	1.567	1527	55	46.086	9.937	−0.981	a
26	SDSS084451.91+282607	1.574	1513	29	45.916	8.698	0.088	a
27	SDSS081227.19+075732	1.574	341	72	46.002	9.895	−1.023	a
28	SDSS091754.44+043652	1.587	−214	31	45.632	9.664	−1.162	a
29	SDSS204538.96−005115	1.590	428	56	45.844	9.180	−0.466	a
30	SDSS014705.42+133210	1.595	1340	40	46.207	9.321	−0.244	a
31	SDSS114023.40+301651	1.599	1462	43	46.423	9.421	−0.128	a
32	SDSS104603.22+112828	1.607	444	44	45.866	9.200	−0.464	a
33	SDSS125140.82+080718	1.607	1681	97	46.091	9.016	−0.055	a
34	SDSS204009.62−065402	1.611	733	97	45.460	8.997	−0.667	a
35	SDSS155240.40+194816	1.613	1183	60	46.044	9.647	−0.733	a
36	SDSS002948.04−095639	1.618	156	24	46.022	8.923	−0.031	a
37	SDSS083850.15+261105	1.618	421	19	46.595	9.420	0.045	a
38	SDSS205554.08+004311	1.624	827	78	45.448	8.957	−0.639	a
39	SDSS135023.68+265243	1.624	1132	36	46.219	9.182	−0.093	a
40	SDSS111949.30+233249	1.626	231	21	46.067	9.558	−0.621	a
41	SDSS004149.64−094705	1.629	571	46	46.187	9.636	−0.579	a
42	SDSS160456.14−001907	1.636	1272	70	46.232	9.435	−0.333	a
43	SDSS141949.39+060654	1.649	2297	62	45.936	9.319	−0.513	a
44	SDSS020044.50+122319	1.654	148	40	45.989	9.260	−0.401	a
45	SDSS142841.97+592552	1.660	352	53	46.089	9.179	−0.220	a
46	SDSS204536.56−010147	1.661	252	35	46.518	9.789	−0.401	a
47	SDSS110240.16+394730	1.664	1591	71	45.953	9.333	−0.510	a
48	SDSS100401.27+423123	1.666	1412	194	46.342	9.280	−0.068	a
49	SDSS213748.44+001220	1.670	79	47	45.815	9.056	−0.371	a
50	SDSS094913.05+175155	1.675	2361	85	46.180	9.493	−0.443	a
51	SDSS153859.45+053705	1.684	975	34	46.055	9.004	−0.079	a
52	SDSS162103.98+002905	1.689	2539	166	46.020	9.452	−0.562	a
53	SDSS0246−0825	1.690	693	51	44.590	8.001	−0.541	b
54	SDSS105951.05+090905	1.690	172	10	46.331	9.402	−0.201	a
55	SDSS041255.16−061210	1.691	1589	77	46.054	9.256	−0.332	a
56	SDSS112542.29+000101	1.692	−111	12	46.234	9.298	−0.194	a
57	SDSS101504.75+123022	1.703	3212	125	46.105	9.298	−0.323	a
58	SDSS122039.45+000427	2.048	870	29	46.391	9.230	0.031	a
59	SDSS143645.80+633637	2.066	398	17	46.723	9.969	−0.376	a
60	SDSS014944.43+150106	2.073	994	22	46.390	9.657	−0.397	a
61	SDSS143148.09+053558	2.095	863	22	46.810	10.561	−0.881	a
62	SDSS142108.71+224117	2.188	976	17	46.813	9.868	−0.185	a

Table 2
(Continued)

#	Name	$z_{\rm fit}$	Velocity Shift (km s^{-1})	Error of Velocity Shift (km s^{-1})	$L^{\dagger}_{5100}$ (erg s^{-1})	$M^{\dagger}_{\rm BH}$ $M_{\odot}$	$L_{\rm bol}/L^{\dagger}_{\rm Edd}$	Reference
(1)	(2)	(3)	(4)	(5)	(6)	(7)	(8)	(9)
63	TON618	2.219	2761	423	47.310	10.610	−0.430	c
64	UM645	2.268	−644	54	46.310	9.458	−0.278	c
65	SDSSJ170102.18+61230	2.290	2474	110	46.340	9.601	−0.391	c
66	SDSSJ115111.20+03404	2.337	74	504	45.580	9.123	−0.673	d
67	SDSSJ144245.66−02425	2.355	1360	144	46.030	9.052	−0.152	d
68	SDSSJ100710.70+04211	2.367	675	121	45.170	8.978	−0.938	d
69	UM642	2.372	83	69	46.290	9.532	−0.372	c
70	SDSSJ125034.41−01051	2.399	378	62	45.410	9.038	−0.758	d
71	SDSSJ095141.33+01325	2.419	−599	33	45.550	8.951	−0.531	d
72	SDSSJ101257.52+02593	2.441	795	103	45.730	8.955	−0.355	d
73	SDSS1138+0314	2.445	250	20	44.810	8.504	−0.824	b
74	SDSSJ025438.37+00213	2.464	−121	49	45.850	9.074	−0.354	d
75	UM629	2.471	709	30	46.560	8.993	0.437	c
76	SDSSJ024933.42−08345	2.494	277	20	46.380	9.537	−0.287	c
77	SDSSJ135445.66+00205	2.514	3126	179	46.490	8.994	0.366	c
78	UM632	2.521	85	20	46.540	9.346	0.064	c
79	SDSSJ100428.43+00182	3.054	399	25	46.440	9.204	0.106	c
80	UM667	3.122	422	71	46.280	9.042	0.108	c
81	SBS1425+606	3.197	2207	44	47.380	10.261	−0.011	c
82	SDSSJ083700.82+35055	3.316	14	22	46.620	9.835	−0.345	e
83	SDSSJ210258.21+00202	3.342	−457	42	45.790	9.519	−0.859	d
84	SDSSJ210311.69−06005	3.344	511	38	46.300	9.627	−0.457	d
85	SDSSJ113838.26−02060	3.347	1406	187	45.790	9.123	−0.463	d
86	SDSSJ083630.55+06204	3.384	1796	219	45.530	8.868	−0.468	d
87	SDSSJ105511.99+02075	3.404	562	67	45.700	9.229	−0.659	d
88	SDSSJ173352.22+54003	3.435	662	39	47.000	9.387	0.483	c
89	SDSSJ115304.62+03595	3.437	43	49	46.040	9.414	−0.504	d
90	SDSSJ115935.64+04242	3.456	213	39	45.920	9.360	−0.570	d
91	SDSSJ153725.36−01465	3.467	626	101	45.980	9.026	−0.176	d
92	SDSSJ164248.71+24030	3.497	710	75	46.410	8.911	0.369	e
93	SDSSJ150620.48+46064	3.503	1784	124	46.380	9.788	−0.538	e
94	SDSSJ075303.33+42313	3.595	−2068	12	46.790	9.895	−0.235	e
95	SDSSJ144144.76+47200	3.643	−212	31	46.560	9.097	0.333	e
96	SDSSJ145408.95+51144	3.648	−1418	29	47.080	9.790	0.160	e
97	SDSSJ101336.37+56153	3.652	1357	353	46.990	10.051	−0.191	e
98	SDSSJ014049.18−08394	3.726	−467	38	46.960	9.797	0.033	e
99	SDSSJ113307.63+52283	3.744	1742	645	46.640	9.026	0.484	e
100	SDSSJ162520.31+22583	3.774	1433	47	46.660	9.700	−0.170	e
101	SDSSJ012403.77+00443	3.827	1309	104	46.830	9.475	0.225	e
102	SDSSJ144542.75+49024	3.881	−221	17	47.120	10.105	−0.115	e
103	SDSSJ132420.83+42255	4.042	−630	100	46.650	9.280	0.240	e
104	SDSSJ105756.28+45555	4.130	324	79	47.240	9.781	0.329	e
105	SDSSJ095511.32+59403	4.364	−2408	52	46.810	9.454	0.226	e
106	SDSSJ083946.22+51120	4.408	−456	214	46.710	9.853	−0.273	e
107	SDSSJ010619.24+00482	4.450	380	37	46.800	10.089	−0.419	e
108	SDSSJ134743.29+49562	4.536	881	282	46.970	10.057	−0.217	e
109	SDSSJ163636.92+31571	4.570	1314	339	46.550	9.832	−0.412	e
110	SDSSJ143835.95+43145	4.669	645	168	47.140	9.864	0.146	e
111	SDSSJ105123.03+35453	4.924	−111	36	46.700	9.634	−0.064	e
112	SDSSJ153650.25+50081	4.941	258	15	46.840	9.592	0.118	e

Note. Column (1): sequence number; column (2): name of high-z QSOs; column (3): redshift used to fit spectrum; columns (4) and (5): shift of the C IV peak wavelength and the error, where the positive value means blueshift; column (6): the luminosity of 5100 Å; columns (7) and (8): $M_{\rm BH}$ and Eddington ratio (in logarithm scale); column (9): references. (a) Shen & Liu (2012), (b) Assef et al. (2011), (c) Shemmer et al. (2004), (d) Netzer et al. (2007), and (e) Jun et al. (2015). † means that the data is from Ge et al. (2016) and the fitting redshifts of UM667 and TON618 are from the NASA/IPAC Extragalactic Database.

The high-z sources were chosen with high S/N in SDSS spectra, have Hβ/[O III], and fall in a good place in the NIR atmospheric window. The high S/N, however, may lead the QSOs with very broad lines and low EW in C IV to be underrepresented in this work. One property of our sample is that PG and high-z QSOs are bright in the UV band. This property reduces the objects that are reddened by circumnuclear dust. The dust might differentially suppress some of the C IV emitting material and the dust-obscured objects may lead a different correlation, but would not be as valid for learning

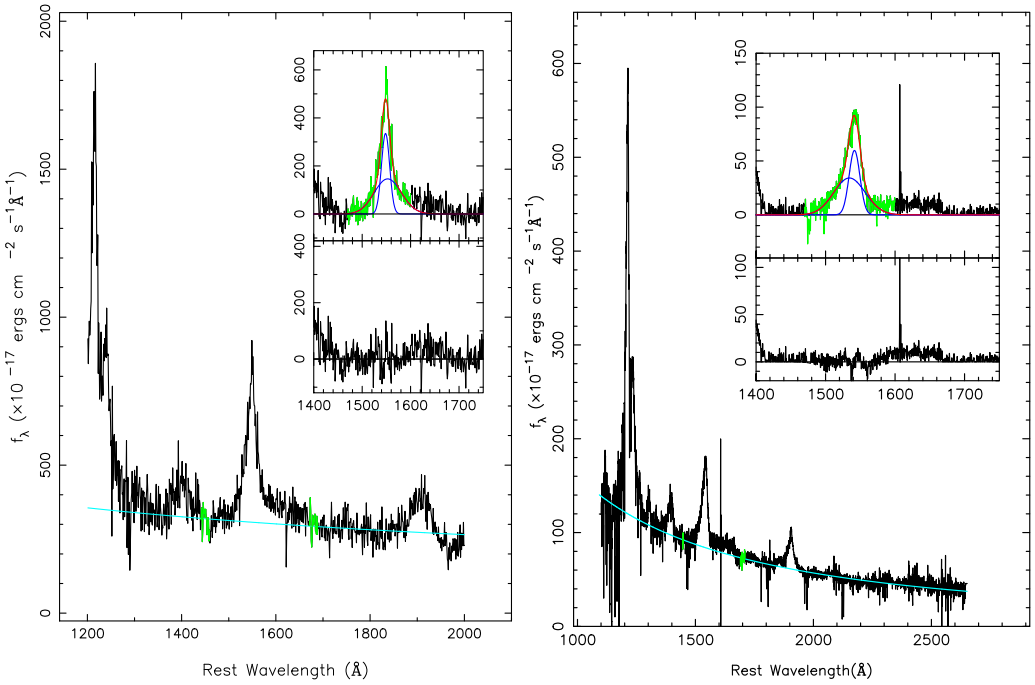

Figure 2. Examples of the UV continuum and emission line fittings for a low-z (left) and a high-z (right) QSO. The original spectra and the fitting windows for the continuum are marked in black and green. The cyan curve is the power law that represents the continuum. The inset shows the fitting of the C IV emission line. The fitting window is also shown in green. The narrow and broad components are marked in blue, and their sum is marked in red. The residual spectrum is shown at the bottom.

about the physical origin of the total C IV profile. It is worth emphasizing that the $M_{\rm BH}$ of the sample is Hβ-based thanks to the infrared observation. This unity enables us to explore the relationship between the C IV blueshift and $L_{\rm Bol}/L_{\rm Edd}$ from low-z to high-z QSOs. In addition, There are 14 radio-loud QSOs in PG QSOs and 11 high-z QSOs, respectively. We do not exclude these objects and will discuss their C IV blueshift in Section 3.

2.2. UV Spectral Decomposition

We need to point out that an average spectrum, weighted by the S/N, is adopted when more than one spectrum is available. We performed least-χ^2 fits to the UV emission line spectra. The χ^2 is determined by the error in the flux. The mean reduced χ^2 are 1.43 and 1.25 for high-z and low-z QSOs, respectively. We list the steps of spectral decomposition as follows. First, the spectra are corrected for Galactic extinction using their A_V values from the NASA/IPAC Extragalactic Database assuming an extinction curve with $R_V = 3.1$ (Cardelli et al. 1989). The extinction-corrected observed spectra are then transformed to the rest frame; no extinction correction is applied for the host galaxy. For PG QSOs, we use the redshifts from Boroson & Green (1992). For high-z QSOs, we adopt the redshifts from Hewett & Wild (2010). For UM667 and TON618, their redshifts are adopted from the NASA/IPAC Extragalactic Database because their redshifts are not available in Hewett & Wild (2010). Next, we fit the continuum using a power-law function in two fitting windows near ∼1450 Å and ∼1710 Å. Finally, the C IV emission line in the continuum-subtracted spectrum is fitted with two Gaussians, one with intermediate velocity width and another with broader width. The FWHM of the two components from BLRs is restricted to be more than 1000 and less than 20,000 km s^{-1}. Simultaneously, we constrain the centers of their profiles to have a shift range of ∼15 Å. The fitting window for the C IV line covers the range of 1470–1600 Å, considering the contamination of He IIλ 1640. It is found that a two-Gaussian fit is adequate for the C IV profile in our low-z and high-z QSOs. Figure 2 shows the examples of the fitting of the continuum and the C IV line. We list the profile parameters of low- and high-z QSOs in Tables 3 and 4.

Wills et al. (1993) and Brotherton et al. (1994) presented a statistical investigation of broad emission-line profiles (such as C IV, Mg II) in QSOs. They proposed a two-component model with a narrow core component (FWHM ∼2000 km s^{-1}) and a broad base component (FWHM ∼7000 km s^{-1}) with a blueshift of ∼1000 km s^{-1} relative to the core component to interpret their results. They suggested that the core-to-base ratio determines the profile of the emission line.

2.3. C IV Blueshift, M_{BH}, and L_{Bol}/L_{Edd}

For the two-Gaussian fitting of the C IV line, the EW(C IV) of the entire profile is calculated by integrating both components and the results are consistent with Wu et al. (2009). The error for EW(C IV) is derived from the errors of the integrated C IV flux and the continuum flux in our fits.

From the reconstructed C IV profile of our two-Gaussian fitting, the C IV peak wavelength is calculated as well as its error. With respect to the rest frame defined by the [O III] emission line or the Balmer emission line (i.e., $z_{\rm sys}$), the C IV blueshift and the error can be calculated following Equations (1) and (2), where c is the speed of light. In Equation (1), λ is the C IV peak wavelength in the rest frame defined by $z_{\rm fit}$ used in our fitting, and $z_{\rm sys}$ is the systemic redshift that is defined by the [O III] or Balmer emission line. The error of the C IV blueshift is determined by the error of the peak wavelength and errors of these two redshifts, which is

Table 3
A Summary of the Fitting Results for PG QSOs

#	Name	$z_{\rm fit}$	$L_{\rm N}$ (erg s^{-1})	FWHM$_{\rm N}$ (km s^{-1})	Peak$_{\rm N}$ (km s^{-1})	$L_{\rm B}$ (erg s^{-1})	FWHM$_{\rm b}$ (km s^{-1})	Peak$_{\rm B}$ (km s^{-1})
(1)	(2)	(3)	(4)	(5)	(6)	(7)	(8)	(9)
1	0003+158	0.450	44.28 ± 0.01	2558 ± 58	5 ± 20	44.67 ± 0.01	12357 ± 223	−847 ± 72
2	0003+199	0.025	42.70 ± 0.01	2349 ± 37	−223 ± 14	42.58 ± 0.01	14492 ± 619	192 ± 188
3	0007+106	0.089	42.97 ± 0.02	3003 ± 122	−170 ± 41	43.17 ± 0.02	15174 ± 026	−509 ± 277
4	0026+129	0.142	42.93 ± 0.02	1536 ± 69	−1006 ± 27	43.50 ± 0.01	14231 ± 590	−932 ± 187
5	0049+171	0.064	42.81 ± 0.14	4556 ± 816	−386 ± 231	42.72 ± 0.16	10520 ± 282	113 ± 501
6	0050+124	0.061	42.61 ± 0.02	2457 ± 87	1369 ± 34	42.80 ± 0.02	20000 ± 521	2905 ± 442
7	0052+251	0.155	43.66 ± 0.02	4134 ± 147	823 ± 43	43.98 ± 0.01	14621 ± 475	207 ± 120
8	0157+001	0.164	43.38 ± 0.02	3688 ± 143	1872 ± 41	43.57 ± 0.02	20000 ± 488	2675 ± 337
9	0804+761	0.100	43.46 ± 0.02	3467 ± 152	−36 ± 52	43.59 ± 0.02	15703 ± 126	466 ± 282
10	0838+770	0.131	42.52 ± 0.27	2208 ± 712	−355 ± 178	43.28 ± 0.06	7955 ± 842	−1149 ± 239
11	0844+349	0.064	42.76 ± 0.06	3535 ± 357	−197 ± 102	43.00 ± 0.05	20000 ± 272	2197 ± 877
12	0921+525	0.035	42.61 ± 0.02	2900 ± 98	−491 ± 30	42.50 ± 0.02	9123 ± 409	−744 ± 115
13	0923+129	0.190	43.80 ± 0.07	2528 ± 218	−389 ± 59	44.05 ± 0.04	6831 ± 443	−320 ± 114
14	0923+201	0.029	41.24 ± 0.10	2695 ± 433	−817 ± 135	41.87 ± 0.03	9901 ± 723	−2057 ± 263
15	0947+396	0.206	43.51 ± 0.02	3030 ± 94	267 ± 30	43.70 ± 0.01	12678 ± 454	−141 ± 132
16	0953+414	0.239	43.81 ± 0.02	2619 ± 86	1336 ± 30	44.07 ± 0.01	11287 ± 318	657 ± 108
17	1011−040	0.058	42.21 ± 0.04	2516 ± 228	−4 ± 81	42.63 ± 0.04	18485 ± 930	−65 ± 747
18	1012+008	0.185	42.42 ± 0.11	2014 ± 359	968 ± 117	43.03 ± 0.03	7275 ± 520	−130 ± 228
19	1022+519	0.045	41.90 ± 0.08	1991 ± 324	−31 ± 115	42.45 ± 0.04	11474 ± 412	412 ± 434
20	1048-090	0.344	43.43 ± 0.22	3098 ± 1229	−989 ± 434	44.13 ± 0.06	15904 ± 346	1199 ± 127
21	1048+342	0.167	42.08 ± 0.41	1840 ± 1048	410 ± 331	42.56 ± 0.17	5803 ± 853	1301 ± 891
22	1049-005	0.357	44.09 ± 0.01	3715 ± 77	−65 ± 26	44.20 ± 0.01	19891 ± 065	−174 ± 252
23	1100+772	0.313	43.65 ± 0.02	2066 ± 86	352 ± 34	44.39 ± 0.01	13162 ± 199	490 ± 69
24	1103-006	0.425	43.20 ± 0.09	2000 ± 294	−55 ± 89	43.88 ± 0.02	7454 ± 396	−5 ± 124
25	1115+407	0.154	43.11 ± 0.04	4013 ± 251	529 ± 77	43.26 ± 0.03	18102 ± 370	−292 ± 590
26	1116+215	0.177	43.90 ± 0.02	3750 ± 134	925 ± 41	44.10 ± 0.01	14092 ± 599	1032 ± 154
27	1119+120	0.049	42.22 ± 0.05	2769 ± 259	−40 ± 91	42.73 ± 0.02	17052 ± 525	620 ± 425
28	1121+422	0.234	43.68 ± 0.01	2297 ± 60	2580 ± 23	43.60 ± 0.02	13480 ± 798	2168 ± 265
29	1149−110	0.049	42.38 ± 0.04	4100 ± 255	570 ± 79	42.44 ± 0.03	15317 ± 652	1795 ± 453
30	1151+117	0.176	43.08 ± 0.04	2406 ± 190	−23 ± 66	43.37 ± 0.03	12044 ± 165	−1729 ± 440
31	1202+281	0.165	43.32 ± 0.01	2565 ± 72	673 ± 27	43.45 ± 0.01	11340 ± 327	1258 ± 111
32	1211+143	0.085	43.20 ± 0.02	2434 ± 94	−196 ± 32	43.22 ± 0.02	10480 ± 678	419 ± 229
33	1216+069	0.334	43.96 ± 0.01	2509 ± 65	281 ± 24	44.35 ± 0.01	15104 ± 376	864 ± 115
34	1226+023	0.158	44.11 ± 0.02	3004 ± 91	622 ± 29	44.34 ± 0.01	10603 ± 308	−492 ± 111
35	1229+204	0.064	42.89 ± 0.03	3632 ± 161	445 ± 48	42.91 ± 0.03	12725 ± 967	−264 ± 272
36	1259+593	0.472	43.53 ± 0.17	4141 ± 862	1700 ± 252	44.13 ± 0.04	11075 ± 739	2905 ± 282
37	1302-102	0.286	43.76 ± 0.02	3234 ± 138	1905 ± 48	44.21 ± 0.01	20000 ± 076	564 ± 282
38	1307+085	0.155	43.52 ± 0.02	3556 ± 131	−264 ± 43	43.71 ± 0.01	15519 ± 821	−256 ± 207
39	1310−108	0.035	42.30 ± 0.04	3193 ± 187	−229 ± 57	42.32 ± 0.04	10706 ± 959	342 ± 276
40	1322+659	0.168	43.36 ± 0.01	2976 ± 53	549 ± 18	43.30 ± 0.01	12769 ± 456	1263 ± 138
41	1341+258	0.087	41.79 ± 0.31	1500 ± 696	−389 ± 199	42.73 ± 0.06	6835 ± 704	−70 ± 280
42	1352+183	0.158	43.30 ± 0.03	3957 ± 187	2256 ± 58	43.39 ± 0.02	16238 ± 294	1635 ± 329
43	1402+261	0.164	43.46 ± 0.03	3895 ± 219	489 ± 72	43.70 ± 0.02	17677 ± 478	1954 ± 385
44	1415+451	0.114	43.05 ± 0.02	3473 ± 125	509 ± 40	43.05 ± 0.02	12530 ± 738	1219 ± 207
45	1416−129	0.129	43.29 ± 0.03	3724 ± 156	−7 ± 51	43.54 ± 0.01	13794 ± 524	313 ± 141
46	1425+267	0.366	43.84 ± 0.15	8094 ± 1032	1555 ± 165	43.99 ± 0.07	20000 ± 970	174 ± 022
47	1426+015	0.086	43.01 ± 0.06	3280 ± 320	49 ± 101	43.55 ± 0.02	14245 ± 929	−221 ± 251
48	1427+480	0.221	43.41 ± 0.02	2374 ± 74	−59 ± 25	43.53 ± 0.01	8412 ± 264	−799 ± 95
49	1435−067	0.129	43.10 ± 0.05	2862 ± 225	227 ± 66	43.20 ± 0.04	9868 ± 053	361 ± 296
50	1440+356	0.077	42.76 ± 0.04	1670 ± 108	468 ± 31	42.95 ± 0.03	5346 ± 350	832 ± 106
51	1444+407	0.267	43.04 ± 0.15	2179 ± 507	748 ± 159	43.81 ± 0.03	7761 ± 508	1440 ± 173
52	1501+106	0.036	42.50 ± 0.03	3389 ± 160	141 ± 52	42.80 ± 0.01	13579 ± 586	617 ± 162
53	1512+370	0.371	43.79 ± 0.02	2595 ± 117	68 ± 41	44.38 ± 0.01	12778 ± 287	1001 ± 96
54	1519+226	0.137	42.96 ± 0.04	2432 ± 188	754 ± 68	43.23 ± 0.03	14662 ± 466	−218 ± 457
55	1534+580	0.030	42.02 ± 0.03	1844 ± 114	−289 ± 40	42.59 ± 0.01	8679 ± 247	323 ± 87
56	1543+489	0.400	43.80 ± 0.03	4802 ± 200	1997 ± 55	43.81 ± 0.03	15044 ± 147	2905 ± 281
57	1545+210	0.266	43.84 ± 0.03	3830 ± 177	230 ± 58	44.21 ± 0.01	15845 ± 617	302 ± 160
58	1612+261	0.131	43.06 ± 0.03	2781 ± 137	−285 ± 47	43.38 ± 0.01	10543 ± 379	−1724 ± 153
59	1613+658	0.129	43.41 ± 0.04	5136 ± 273	574 ± 74	43.53 ± 0.03	14,978 ± 225	−1793 ± 502
60	1617+175	0.114	42.50 ± 0.10	2810 ± 458	354 ± 146	43.10 ± 0.03	12214 ± 049	415 ± 308
61	1626+554	0.133	43.25 ± 0.03	3366 ± 168	569 ± 54	43.45 ± 0.02	13619 ± 804	−74 ± 239
62	2130+099	0.061	42.74 ± 0.03	2226 ± 118	−518 ± 40	42.94 ± 0.02	10361 ± 670	−337 ± 211

Table 3
(Continued)

#	Name	z_{fit}	L_N (erg s^{-1})	FWHM$_N$ (km s^{-1})	Peak$_N$ (km s^{-1})	L_B (erg s^{-1})	FWHM$_b$ (km s^{-1})	Peak$_B$ (km s^{-1})
(1)	(2)	(3)	(4)	(5)	(6)	(7)	(8)	(9)
63	2209+184	0.070	42.60 ± 0.08	4963 ± 597	758 ± 167	42.95 ± 0.03	20000 ± 454	687 ± 628
64	2214+139	0.067	42.55 ± 0.06	3307 ± 308	−100 ± 95	42.86 ± 0.03	10833 ± 746	929 ± 241
65	2251+113	0.323	43.90 ± 0.02	3664 ± 96	−365 ± 34	44.24 ± 0.01	18153 ± 603	285 ± 147
66	2304+042	0.042	41.97 ± 0.03	2338 ± 148	−69 ± 51	42.36 ± 0.02	10493 ± 470	682 ± 160
67	2308+098	0.432	43.94 ± 0.02	3302 ± 99	−159 ± 35	44.43 ± 0.01	16611 ± 443	−1607 ± 148

Note. Column (1): sequence number; column (2): name of PG QSOs; column (3): redshift from Schmidt & Green (1983); columns (4)–(9): the profile fitting parameters of C IV (luminosity, FWHM, and peak). Subscript N and B indicate narrow and broad components, respectively.

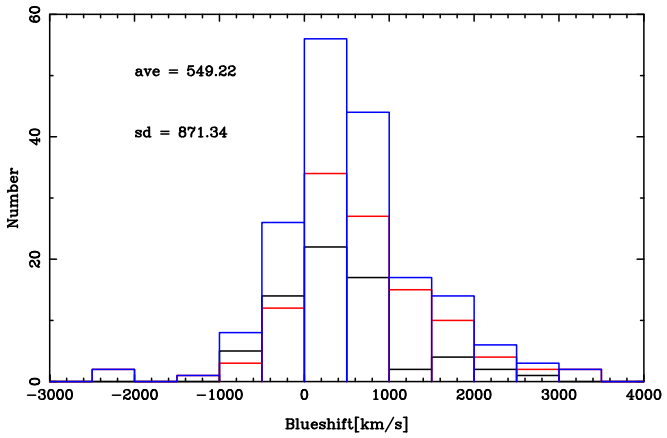

Figure 3. Distributions of the velocity shift of the whole C IV emission line for PG QSOs (black), high-z QSOs (red), and the entire sample (blue). The average and standard deviation of the distribution are marked on the top right. The positive value denotes the blueshift in units of km s^{-1}.

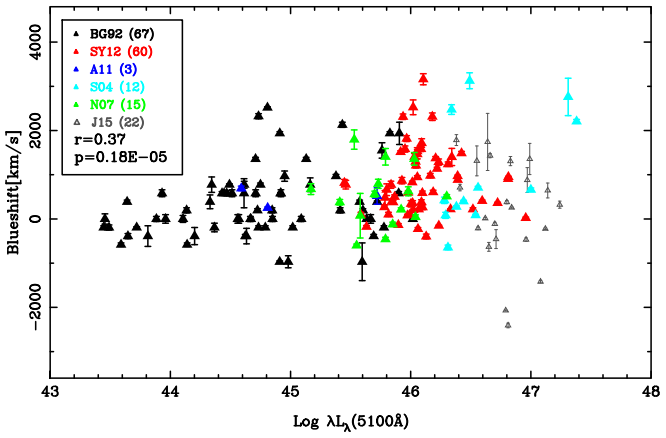

Figure 4. C IV velocity shift vs. the luminosity at 5100 Å for our sample. The points with different colors represent that these sources are form different literatures and the number in the brackets indicates the number of objects used here as indicated in the legend. A subsample without the sources from Jun et al. (2015; gray points) is used to do the Spearman correlation test. The Spearman correlation coefficient and the probability of the null hypothesis are 0.37 and 1.8×10^{-6}, respectively.

related to the spectral resolution during observations.

$$v = \left(\frac{\lambda(1+z_{\rm fit})}{1+z_{\rm sys}} - 1549\right)\frac{c}{1549} \quad (1)$$

$$(\delta v)^2 = \left(\left(\frac{\delta\lambda(1+z_{\rm fit})}{1+z_{\rm sys}}\right)^2 + \left(\frac{\lambda\delta z_{\rm fit}}{1+z_{\rm sys}}\right)^2 + \left(\frac{\lambda\delta z_{\rm sys}(1+z_{\rm fit})}{(1+z_{\rm sys})^2}\right)^2\right) \times \left(\frac{c}{1549}\right)^2. \quad (2)$$

We calculate the error of the C IV blueshift according to the error transfer formula (Equation (2)). For PG QSOs, the resolution of the optical spectra is 6.5 Å corresponding to ∼400 km s^{-1}. The resolution of the UV spectra is ∼460 km s^{-1} and ∼1200 km s^{-1} for *HST* and *IUE* data, respectively. For a high-z QSO ($z = 2$) with an infrared spectral resolution of $R \sim 100$, the uncertainty of its blueshift is ∼1000 km s^{-1}. If $R \sim 3000$, then the uncertainty of its blueshift is ∼30 km s^{-1}. For SDSS UV spectra, $R \sim 2000$, and the uncertainty of the blueshifts is ∼50 km s^{-1}. Typically, the centroid of a well-shaped emission line can be determined to at least 0.1 or better of the spectral resolution. The larger uncertainty in the C IV blueshift comes from noise in the broad emission line profiles (Boroson & Green 1992). We can therefore ignore the effect of spectral resolution on the error of the blueshift. For that reason, we do not consider the uncertainties from the spectral resolution and the two redshifts, zfit and z_{sys}, for either low- or high-z QSOs. The error of the C IV blueshift is calculated only from the error of the fit of the C IV peak wavelength.

For our sample of low-z and high-z QSOs, Ge et al. (2016) has computed the Hβ-based single-epoch SMBH mass, $M_{\rm BH}$, and host-corrected $L_{\rm Bol}/L_{\rm Edd}$. They estimated the bolometric luminosity based on a constant bolometric correction (9.26) and host-corrected L (5100Å; see Ge et al. 2016 for details) . We use these parameters to investigate the relation with the C IV blueshift. In order to investigate the bias in C IV-based $M_{\rm BH}$, we measure the C IV FWHM from the best-fitting C IV profile, as well as the luminosity at 1350 Å. The C IV-based SMBH mass is calculated following the formula of Vestergaard & Peterson (2006).

3. Result and Discussion

3.1. Blueshift of the Whole C IV Emission Line

Based on the rest frame defined by [O III] λ5007 or other low-ionization emission lines (e.g., Hβ), the blueshift of the whole C IV profile is investigated for our sample. Figure 3 shows the distribution of the C IV velocity shift for low-z PG QSOs (black), high-z QSOs (red), and our sample (blue). Most objects exhibit blueshift (positive values) and the biggest blueshift is up to ∼3200 km s^{-1}. The average and standard deviation of the

Table 4
A Summary of the Fitting Results for High-z QSOs

#	Name	$z_{\rm fit}$	$L_{\rm N}$ (erg s^{-1})	FWHM$_{\rm N}$ (km s^{-1})	Peak$_{\rm N}$ (km s^{-1})	$L_{\rm B}$ (erg s^{-1})	FWHM$_{\rm b}$ (km s^{-1})	Peak$_{\rm B}$ (km s^{-1})
(1)	(2)	(3)	(4)	(5)	(6)	(7)	(8)	(9)
1	SDSS225800.02−084143	1.496	45.54 ± 0.05	3753 ± 226	807 ± 80	46.00 ± 0.07	16574 ± 1581	2905 ± 131
2	SDSS035856.73−054023	1.506	45.04 ± 0.11	3454 ± 446	1007 ± 133	45.24 ± 0.08	8050 ± 676	−1079 ± 614
3	SDSS133321.90+005824	1.511	45.64 ± 0.02	2794 ± 86	361 ± 30	46.25 ± 0.01	12624 ± 247	−910 ± 80
4	SDSS081331.28+254503	1.513	46.42 ± 0.02	3394 ± 83	843 ± 19	46.48 ± 0.01	10223 ± 406	1349 ± 92
5	SDSS152111.86+470539	1.517	45.73 ± 0.02	2664 ± 74	409 ± 25	45.98 ± 0.01	12977 ± 565	21 ± 163
6	FBQ1633+3134	1.522	45.32 ± 0.12	2265 ± 256	2905 ± 185	45.69 ± 0.05	3073 ± 239	571 ± 175
7	SDSS085543.26+002908	1.525	45.43 ± 0.02	2664 ± 93	149 ± 30	45.82 ± 0.01	12712 ± 494	770 ± 143
8	SDSS123355.21+031327	1.528	45.41 ± 0.05	4380 ± 261	954 ± 71	45.99 ± 0.01	14673 ± 693	1088 ± 164
9	SDSS104910.31+143227	1.540	45.74 ± 0.02	4331 ± 112	1265 ± 29	45.67 ± 0.02	12566 ± 750	1082 ± 160
10	SDSS154212.90+111226	1.540	45.93 ± 0.14	5052 ± 521	1315 ± 106	45.43 ± 0.47	9174 ± 5240	−2905 ± 310
11	SDSS143230.57+012435	1.542	45.64 ± 0.04	4443 ± 248	1454 ± 67	45.82 ± 0.03	17032 ± 2317	2095 ± 516
12	SDSS074029.82+281458	1.545	45.82 ± 0.03	3925 ± 136	970 ± 36	46.09 ± 0.01	13315 ± 662	2198 ± 163
13	SDSS081344.15+152221	1.545	45.62 ± 0.07	4693 ± 351	1349 ± 75	45.72 ± 0.04	13894 ± 2885	2905 ± 962
14	SDSS082146.22+571226	1.546	45.99 ± 0.02	4771 ± 167	1596 ± 49	45.74 ± 0.08	20000 ± 5902	2905 ± 753
15	SDSS171030.20+602347	1.549	45.69 ± 0.03	3888 ± 172	566 ± 54	45.98 ± 0.02	11419 ± 400	−1210 ± 177
16	SDSS123442.16+052126	1.550	45.73 ± 0.03	4507 ± 188	1091 ± 52	45.86 ± 0.02	13,433 ± 901	267 ± 213
17	SDSS015733.87−004824	1.551	45.56 ± 0.09	6586 ± 562	1578 ± 162	45.27 ± 0.17	13578 ± 2649	−2905 ± 531
18	SDSS101447.54+521320	1.552	45.71 ± 0.04	4261 ± 210	689 ± 54	45.59 ± 0.04	13448 ± 1971	458 ± 395
19	SDSS135439.70+301649	1.553	45.69 ± 0.02	4852 ± 155	1182 ± 45	45.54 ± 0.04	19307 ± 3631	−406 ± 755
20	SDSS223246.80+134702	1.557	45.49 ± 0.02	2659 ± 106	155 ± 34	46.14 ± 0.01	10761 ± 182	−27 ± 54
21	SDSS100930.51+023052	1.557	45.47 ± 0.03	4986 ± 239	343 ± 52	45.65 ± 0.02	20000 ± 2813	−75 ± 359
22	SDSS124006.70+474003	1.561	45.68 ± 0.03	3652 ± 146	495 ± 40	45.94 ± 0.02	9284 ± 296	1512 ± 96
23	SDSS093318.49+141340	1.561	45.86 ± 0.02	4378 ± 128	834 ± 53	45.96 ± 0.02	12342 ± 402	−1432 ± 192
24	SDSS094126.49+044328	1.567	45.54 ± 0.03	3350 ± 146	284 ± 44	45.97 ± 0.01	11759 ± 375	−509 ± 108
25	SDSS113829.33+040101	1.567	45.06 ± 0.05	1406 ± 151	474 ± 55	46.11 ± 0.01	8871 ± 198	1281 ± 72
26	SDSS084451.91+282607	1.574	45.83 ± 0.02	4686 ± 105	1307 ± 29	45.69 ± 0.02	20000 ± 2320	−60 ± 506
27	SDSS081227.19+075732	1.574	45.37 ± 0.05	3321 ± 229	315 ± 72	45.80 ± 0.02	9313 ± 298	−1703 ± 174
28	SDSS091754.44+043652	1.587	45.74 ± 0.02	2862 ± 94	248 ± 31	46.22 ± 0.01	9575 ± 150	−954 ± 59
29	SDSS204538.96−005115	1.590	45.48 ± 0.04	3077 ± 178	844 ± 56	45.84 ± 0.02	12037 ± 640	244 ± 179
30	SDSS014705.42+133210	1.595	45.64 ± 0.03	3659 ± 139	969 ± 40	46.02 ± 0.01	12681 ± 386	1740 ± 107
31	SDSS114023.40+301651	1.599	46.01 ± 0.03	4511 ± 161	1775 ± 43	46.31 ± 0.01	13585 ± 424	2205 ± 100
32	SDSS104603.22+112828	1.607	45.61 ± 0.03	3861 ± 156	991 ± 44	45.78 ± 0.02	12578 ± 607	422 ± 168
33	SDSS125140.82+080718	1.607	45.53 ± 0.08	3991 ± 359	1751 ± 97	46.14 ± 0.02	9438 ± 278	2905 ± 103
34	SDSS204009.62−065402	1.611	45.09 ± 0.07	2830 ± 328	647 ± 97	45.45 ± 0.03	10093 ± 860	433 ± 246
35	SDSS155240.40+194816	1.613	45.65 ± 0.04	4452 ± 213	1172 ± 60	45.86 ± 0.02	13716 ± 776	−544 ± 270
36	SDSS002948.04−095639	1.618	45.90 ± 0.01	3728 ± 81	802 ± 24	45.92 ± 0.01	13304 ± 527	−36 ± 150
37	SDSS083850.15+261105	1.618	46.34 ± 0.01	3959 ± 57	987 ± 19	46.45 ± 0.01	16928 ± 446	1930 ± 112
38	SDSS205554.08+004311	1.624	45.45 ± 0.05	4117 ± 274	1020 ± 78	45.54 ± 0.04	15466 ± 2008	1493 ± 469
39	SDSS135023.68+265243	1.624	45.69 ± 0.02	3036 ± 108	834 ± 36	46.11 ± 0.01	12265 ± 307	2041 ± 105
40	SDSS111949.30+233249	1.626	45.39 ± 0.02	1548 ± 61	417 ± 21	45.92 ± 0.01	6682 ± 207	428 ± 65
41	SDSS004149.64−094705	1.629	45.88 ± 0.02	4764 ± 152	650 ± 46	46.30 ± 0.01	20000 ± 777	2140 ± 168
42	SDSS160456.14−001907	1.636	45.70 ± 0.04	4019 ± 243	1377 ± 70	46.16 ± 0.02	12523 ± 462	2422 ± 144
43	SDSS141949.39+060654	1.649	45.86 ± 0.04	5696 ± 251	2020 ± 62	45.88 ± 0.03	18045 ± 1835	2905 ± 346
44	SDSS020044.50+122319	1.654	45.65 ± 0.02	3101 ± 116	719 ± 40	45.94 ± 0.01	12268 ± 448	−1676 ± 203
45	SDSS142841.97+592552	1.660	45.47 ± 0.04	3085 ± 190	1031 ± 53	45.96 ± 0.01	9632 ± 313	1536 ± 90
46	SDSS204536.56−010147	1.661	46.37 ± 0.02	4861 ± 119	981 ± 35	46.34 ± 0.02	13112 ± 515	−1416 ± 246
47	SDSS110240.16+394730	1.664	45.78 ± 0.04	5992 ± 288	1948 ± 71	45.72 ± 0.03	18326 ± 2498	−423 ± 821
48	SDSS100401.27+423123	1.666	45.55 ± 0.19	4071 ± 642	1570 ± 194	46.14 ± 0.05	7435 ± 282	2859 ± 179
49	SDSS213748.44+001220	1.670	45.36 ± 0.03	2630 ± 138	659 ± 47	44.58 ± 0.26	11711 ± 10655	2905 ± 887
50	SDSS094913.05+175155	1.675	45.59 ± 0.04	4182 ± 295	1877 ± 85	46.18 ± 0.01	15051 ± 484	2705 ± 125
51	SDSS153859.45+053705	1.684	45.76 ± 0.02	3515 ± 112	1066 ± 34	45.81 ± 0.02	12147 ± 692	940 ± 176
52	SDSS162103.98+002905	1.689	45.20 ± 0.15	4544 ± 619	1493 ± 166	45.49 ± 0.08	9407 ± 821	2765 ± 348
53	SDSS0246−0825	1.690	45.40 ± 0.05	2614 ± 177	547 ± 51	46.00 ± 0.01	7018 ± 166	1428 ± 63
54	SDSS105951.05+090905	1.690	46.35 ± 0.01	2421 ± 28	521 ± 10	46.47 ± 0.01	11605 ± 172	647 ± 54
55	SDSS041255.16−061210	1.691	45.75 ± 0.06	4507 ± 264	1159 ± 77	46.07 ± 0.03	10093 ± 351	2780 ± 164
56	SDSS112542.29+000101	1.692	46.25 ± 0.01	2172 ± 24	301 ± 12	46.10 ± 0.01	8868 ± 187	−1635 ± 121
57	SDSS101504.75+123022	1.703	45.68 ± 0.10	5866 ± 591	2540 ± 125	46.04 ± 0.04	15706 ± 1470	2905 ± 241
58	SDSS122039.45+000427	2.048	46.29 ± 0.02	4344 ± 104	1058 ± 29	46.54 ± 0.01	14361 ± 377	890 ± 89
59	SDSS143645.80+633637	2.066	46.38 ± 0.01	2989 ± 54	336 ± 17	46.73 ± 0.01	11201 ± 146	355 ± 42
60	SDSS014944.43+150106	2.073	46.52 ± 0.01	5495 ± 89	1488 ± 22	46.51 ± 0.01	18675 ± 891	656 ± 188
61	SDSS143148.09+053558	2.095	46.54 ± 0.01	3676 ± 73	445 ± 22	46.82 ± 0.01	14190 ± 293	348 ± 77
62	SDSS142108.71+224117	2.188	46.88 ± 0.01	4322 ± 51	655 ± 17	46.83 ± 0.01	14387 ± 329	944 ± 78

Table 4
(Continued)

#	Name	z_{fit}	L_N (erg s^{-1})	FWHM$_N$ (km s^{-1})	Peak$_N$ (km s^{-1})	L_B (erg s^{-1})	FWHM$_b$ (km s^{-1})	Peak$_B$ (km s^{-1})
(1)	(2)	(3)	(4)	(5)	(6)	(7)	(8)	(9)
63	TON618	2.219	45.44 ± 0.35	3083 ± 1398	1331 ± 423	46.66 ± 0.02	8620 ± 362	2905 ± 179
64	UM645	2.268	46.35 ± 0.03	4677 ± 202	360 ± 54	46.35 ± 0.02	18706 ± 2100	172 ± 480
65	SDSSJ170102.18+61230	2.290	45.99 ± 0.05	4196 ± 286	1437 ± 110	46.03 ± 0.05	13274 ± 1328	2905 ± 466
66	SDSSJ115111.20+03404	2.337	45.21 ± 0.68	1847 ± 602	292 ± 504	45.18 ± 0.75	2483 ± 1817	−1139 ± 825
67	SDSSJ144245.66−02425	2.355	45.80 ± 0.11	4455 ± 585	1322 ± 144	45.79 ± 0.12	10632 ± 1897	369 ± 595
68	SDSSJ100710.70+04211	2.367	45.79 ± 0.07	4727 ± 448	1054 ± 121	45.64 ± 0.09	14292 ± 3832	−1102 ± 471
69	UM642	2.372	46.34 ± 0.03	3865 ± 190	1042 ± 69	46.63 ± 0.01	14602 ± 680	224 ± 187
70	SDSSJ125034.41−01051	2.399	45.79 ± 0.04	2905 ± 179	569 ± 62	46.08 ± 0.02	9848 ± 501	−610 ± 187
71	SDSSJ095141.33+01325	2.419	45.52 ± 0.03	1693 ± 95	159 ± 33	46.11 ± 0.01	8025 ± 226	−727 ± 86
72	SDSSJ101257.52+02593	2.441	45.88 ± 0.06	4782 ± 371	1374 ± 103	45.91 ± 0.05	14478 ± 1968	2620 ± 567
73	SDSS1138+0314	2.445	46.42 ± 0.01	2195 ± 36	517 ± 20	46.43 ± 0.01	15787 ± 474	917 ± 146
74	SDSSJ025438.37+00213	2.464	45.92 ± 0.03	2525 ± 152	544 ± 49	46.06 ± 0.02	11724 ± 803	888 ± 250
75	UM629	2.471	46.55 ± 0.02	4062 ± 100	1604 ± 30	46.64 ± 0.01	14900 ± 678	2905 ± 201
76	SDSSJ024933.42−08345	2.494	46.42 ± 0.01	2576 ± 61	520 ± 20	46.65 ± 0.01	9979 ± 266	1760 ± 117
77	SDSSJ135445.66+00205	2.514	46.08 ± 0.12	5431 ± 647	1326 ± 179	46.46 ± 0.05	11463 ± 685	2905 ± 309
78	UM632	2.521	46.29 ± 0.01	1891 ± 55	409 ± 20	46.84 ± 0.01	11871 ± 280	382 ± 87
79	SDSSJ100428.43+00182	3.054	46.68 ± 0.02	2543 ± 76	925 ± 25	46.89 ± 0.01	8744 ± 243	1983 ± 88
80	UM667	3.122	46.36 ± 0.04	4282 ± 224	−455 ± 71	46.72 ± 0.02	13838 ± 562	1597 ± 212
81	SBS1425+606	3.197	47.50 ± 0.02	5556 ± 166	1744 ± 44	47.80 ± 0.01	15477 ± 360	2535 ± 77
82	SDSSJ083700.82+35055	3.316	47.00 ± 0.01	3506 ± 69	1084 ± 22	47.03 ± 0.01	13875 ± 482	2429 ± 153
83	SDSSJ210258.21+00202	3.342	45.73 ± 0.05	1000 ± 111	544 ± 42	46.36 ± 0.03	9442 ± 777	467 ± 281
84	SDSSJ210311.69−06005	3.344	46.75 ± 0.02	4099 ± 151	1037 ± 38	46.87 ± 0.02	15152 ± 789	685 ± 200
85	SDSSJ113838.26−02060	3.347	45.98 ± 0.27	3823 ± 923	1088 ± 187	46.36 ± 0.11	8514 ± 1396	853 ± 291
86	SDSSJ083630.55+06204	3.384	46.16 ± 0.12	4962 ± 779	965 ± 219	46.25 ± 0.09	17208 ± 6637	−2905 ± 248
87	SDSSJ105511.99+02075	3.404	46.58 ± 0.04	4317 ± 237	1423 ± 67	46.77 ± 0.02	16550 ± 1517	426 ± 384
88	SDSSJ173352.22+54003	3.435	46.99 ± 0.02	3271 ± 116	995 ± 39	47.24 ± 0.01	10278 ± 281	2905 ± 142
89	SDSSJ115304.62+03595	3.437	46.19 ± 0.03	1763 ± 119	786 ± 49	46.35 ± 0.04	13901 ± 1702	2454 ± 652
90	SDSSJ115935.64+04242	3.456	46.25 ± 0.03	1662 ± 106	527 ± 39	46.95 ± 0.01	10541 ± 295	−112 ± 107
91	SDSSJ153725.36−01465	3.467	46.54 ± 0.04	4532 ± 326	1567 ± 101	46.79 ± 0.03	20000 ± 2528	2905 ± 583
92	SDSSJ164248.71+24030	3.497	46.85 ± 0.03	5217 ± 255	1754 ± 75	47.11 ± 0.02	20000 ± 1567	2905 ± 317
93	SDSSJ150620.48+46064	3.503	46.79 ± 0.06	5562 ± 401	408 ± 124	46.97 ± 0.04	14111 ± 907	2905 ± 444
94	SDSSJ075303.33+42313	3.595	47.00 ± 0.01	2195 ± 35	212 ± 12	47.28 ± 0.01	10746 ± 199	512 ± 61
95	SDSSJ144144.76+47200	3.643	46.86 ± 0.02	2604 ± 95	1270 ± 31	47.17 ± 0.01	12317 ± 485	1713 ± 165
96	SDSSJ145408.95+51144	3.648	47.28 ± 0.02	3716 ± 96	1009 ± 29	47.46 ± 0.01	11995 ± 323	2043 ± 113
97	SDSSJ101336.37+56153	3.652	46.46 ± 0.17	3482 ± 872	2144 ± 353	47.11 ± 0.03	10524 ± 586	1721 ± 154
98	SDSSJ014049.18−08394	3.726	47.14 ± 0.02	3867 ± 124	1763 ± 38	47.10 ± 0.02	13486 ± 848	2905 ± 260
99	SDSSJ113307.63+52283	3.744	46.81 ± 0.77	7358 ± 3905	1857 ± 645	46.63 ± 0.93	15605 ± 30749	2905 ± 855
100	SDSSJ162520.31+22583	3.774	46.91 ± 0.03	2850 ± 146	1034 ± 47	47.36 ± 0.01	10635 ± 315	1926 ± 106
101	SDSSJ012403.77+00443	3.827	46.73 ± 0.07	3436 ± 329	712 ± 104	47.47 ± 0.01	9418 ± 213	2578 ± 117
102	SDSSJ144542.75+49024	3.881	47.37 ± 0.01	2080 ± 50	403 ± 17	47.77 ± 0.01	8290 ± 124	1524 ± 55
103	SDSSJ132420.83+42255	4.042	46.94 ± 0.04	4155 ± 305	1225 ± 100	47.56 ± 0.01	20000 ± 1016	2905 ± 271
104	SDSSJ105756.28+45555	4.130	47.18 ± 0.05	3412 ± 234	57 ± 79	47.76 ± 0.01	9599 ± 205	2099 ± 118
105	SDSSJ095511.32+59403	4.364	47.28 ± 0.04	3347 ± 173	1112 ± 52	47.57 ± 0.02	10775 ± 468	1958 ± 176
106	SDSSJ083946.22+51120	4.408	46.52 ± 0.21	2339 ± 680	400 ± 214	47.14 ± 0.05	7452 ± 961	1614 ± 452
107	SDSSJ010619.24+00482	4.450	47.41 ± 0.03	2432 ± 112	915 ± 37	47.41 ± 0.03	7122 ± 398	2062 ± 193
108	SDSSJ134743.29+49562	4.536	47.14 ± 0.25	4163 ± 964	699 ± 282	47.55 ± 0.10	7979 ± 600	2448 ± 542
109	SDSSJ163636.92+31571	4.570	46.60 ± 0.28	2352 ± 1058	1201 ± 339	47.24 ± 0.07	8397 ± 1327	2185 ± 574
110	SDSSJ143835.95+43145	4.669	47.28 ± 0.11	3784 ± 560	297 ± 168	47.66 ± 0.05	9529 ± 599	2905 ± 494
111	SDSSJ105123.03+35453	4.924	46.99 ± 0.04	1604 ± 110	463 ± 36	47.40 ± 0.02	4798 ± 159	1764 ± 103
112	SDSSJ153650.25+50081	4.941	47.15 ± 0.02	1281 ± 47	1298 ± 15	47.68 ± 0.01	4974 ± 90	1487 ± 28

Note. Column (1): sequence number; column (2): name of high-z QSOs; column (3): redshift used to fit spectrum; columns (4)–(9): the profile fitting parameters of C IV (luminosity, FWHM, and peak). Subscript N and B indicate narrow and broad components, respectively. Note that the profile parameters may be problematic for QSOs with $z < 1.7$ due to the incompleteness of the C IV profile.

distribution are 549.22 km s^{-1} and 871.34 km s^{-1}, respectively. We note that Coatman et al. (2017) showed a more extended tail of blueshift (>3000 km s^{-1}) based on the rest frame defined by Balmer lines, which may originate from a different definition of systemic redshift in our work and their work. We also note that the blueshift of PG and high-z QSOs are ∼300 km s^{-1} and ∼700 km s^{-1} ,respectively. The lower blueshift for PG QSOs is correlative with the lower bolometric luminosity, which reduces the average blueshift of our sample.

We explore the relationship between the C IV velocity shift and the continuum luminosity at 5100 Å. Figure 4 shows that there is a weak correlation between the C IV blueshift and

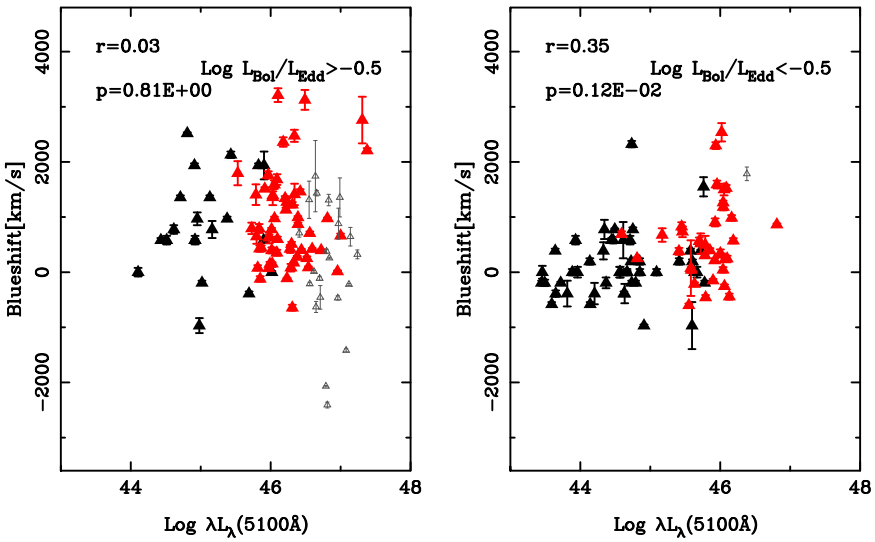

Figure 5. Relationship between the C IV velocity shift and L (5100Å) in high $L_{\rm Bol}/L_{\rm Edd}$ (left) and low $L_{\rm Bol}/L_{\rm Edd}$ (right). The black and red points represent low-z and high-z QSOs (including Shemmer et al. 2004; Netzer et al. 2007; Assef et al. 2011; Shen & Liu 2012), respectively. The gray points are from Jun et al. (2015). The method of calculating Spearman correlation coefficients is the same as Figure 4.

L (5100 Å) for the sample, where $r = 0.23$ and $p = 2.3 \times 10^{-3}$. The weak correlation may be due to the mixing of $L_{\rm Bol}/L_{\rm Edd}$. Figure 5 shows the relationship between the C IV blueshift and the continuum luminosity at 5100 Å in different $L_{\rm Bol}/L_{\rm Edd}$ bins. We can see the correlation coefficient for low $L_{\rm Bol}/L_{\rm Edd}$ is higher than that of high $L_{\rm Bol}/L_{\rm Edd}$ (0.38 versus 0.16). The result is consistent with that given by Shen et al. (2016). They investigated the velocity shifts of QSO emission lines from the SDSS reverberation mapping project and found that the velocity shift of C IV relative to Mg II has a stronger luminosity dependence than other emission lines (such as [O II], [O III], and Mg II). It is worth noting that our correlation test in right panel of Figure 5 agrees with Shen et al. (2016; $r \sim 0.4$) when considering only the objects with the continuum luminosity less than $\sim 10^{46}$ erg s^{-1}. In this work, there are 14 radio-loud QSOs in PG QSOs and 11 high-z QSOs, respectively. We find that the correlation coefficients for the C IV blueshift and L (5100 Å)/$L_{\rm Bol}/L_{\rm Edd}$ only increase by 0.06 after excluding the radio-loud QSOs. Therefore, radio-loud QSOs in our sample do not significantly affect our results. These radio-loud QSOs have, on average, smaller C IV blueshift (132 km s^{-1}) than those of radio-quiet QSOs (616 km s^{-1}), which is consistent with the result of Richards et al. (2011).

Figure 6 displays the relationship between the C IV blueshift and $L_{\rm Bol}/L_{\rm Edd}$ for the sample, where $r = 0.27$ and $p = 3.3 \times 10^{-4}$. It is found that the relation will become flat when we go to higher $L_{\rm Bol}/L_{\rm Edd}$. The possible explanation for the flat relation is that the size of BLR does not depend on the luminosity in high accretion rate QSOs (Du et al. 2018). Some studies have suggested that the accretion disk will become geometrically thick (e.g., slim disk) in the high accretion rate regime, which significantly reduces the amount of the ionizing photons reaching the BLR, and then leads to saturated luminosity (Wang & Zhou 1999; Wang et al. 2014). The self-shadowing effect of slim disks reduces the radiation pressure and flattens the relation between the C IV blueshift and $L_{\rm Bol}/L_{\rm Edd}$ or L (5100 Å). Ge et al. (2016) estimated the intrinsic total luminosity of low-z and high-z QSOs based on a simple scaling factor. Such a rough calculation may not reveal the intrinsic relations of these parameters. Actually, the reradiation from dust has great

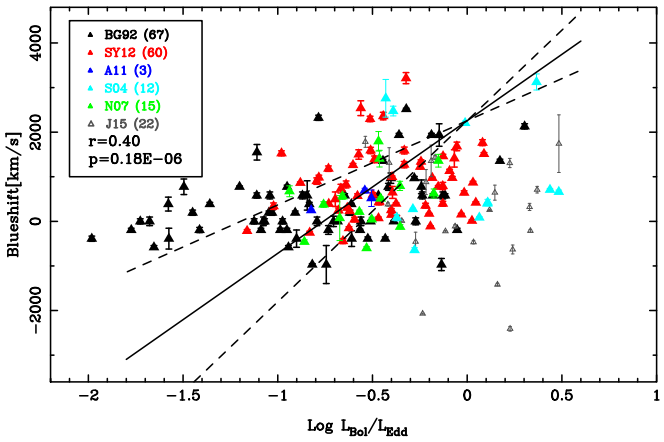

Figure 6. Relationship between the C IV velocity shift and $L_{\rm Bol}/L_{\rm Edd}$. All of the symbols and labels are the same as Figure 4. The solid line is the best fit of the Bivariate Correlated Errors and intrinsic Scatter (BCES) bisector (removing the sources from Jun et al. 2015) and the dashed lines are the best fit of the BCES bisector with 2σ variance. 0.3 dex is adopted as the typical error of $L_{\rm Bol}/L_{\rm Edd}$ in the fitting.

contamination to the intrinsic AGN luminosity, thus the $L_{\rm Bol}/L_{\rm Edd}$. Marconi et al. (2004) constructed a spectral energy distribution (SED) template spectrum without the infrared bump based on α (optical-UV spectral index) and $\alpha_{\rm ox}$ (optical-X-ray spectral index). They derived the bolometric correction, which depends on monochromatic luminosity from the templates. For our sample, the range of luminosity at 5100 Å is from 10^{43} to 10^{47} erg s^{-1} and the corresponding bolometric correction is between 5 and 9. So in this work, we may overestimate the $L_{\rm Bol}/L_{\rm Edd}$, thus affecting our results. We also find an increasing correlation between the C IV blueshift and the luminosity of 5100 Å ($L_{\rm Bol}/L_{\rm Edd}$) when we remove the sources from Jun et al. (2015) in our sample. The correlation coefficient and the probability of the null hypothesis are 0.37 (0.40) and 1.8×10^{-6} (1.8×10^{-7}), respectively. Simultaneously, we fitted the relationship between the C IV blueshift and $L_{\rm Bol}/L_{\rm Edd}$ (solid

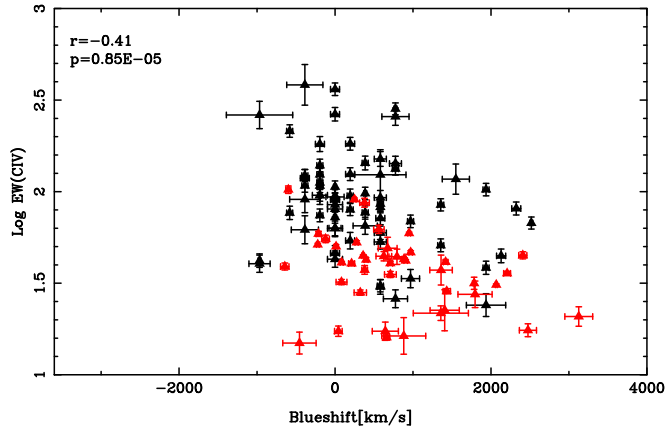

Figure 7. Relationship between the C IV velocity shift and EW(C IV). The correlation coefficients are marked at the top of the panel. PG QSOs and high-z QSOs with C IV S/N $>$ 5 and $z > 2.0$ are marked with black and red points.

line) in Figure 6. The formula for the best fit is

$$V(\mathrm{C\,IV}) = 2257.90(\pm 312.17) + 2974.10(\pm 548.23) \times \log L_{\mathrm{bol}}/L_{\mathrm{Edd}}. \quad (3)$$

The resolution of the infrared spectra from Jun et al. (2015) is the lowest ($R \sim 200$), which can also affect the precision of $L_{\mathrm{Bol}}/L_{\mathrm{Edd}}$. In addition, Wang et al. (2011) presented a comparison of kinematics between C IV and Mg II emission lines using SDSS data. They found that the blueshift of C IV is strongly correlative with $L_{\mathrm{Bol}}/L_{\mathrm{Edd}}$, which is especially prominent in the high $L_{\mathrm{Bol}}/L_{\mathrm{Edd}}$ regime. The same result was found by Sun et al. (2018) recently, who used multi-epoch SDSS spectra to investigate the dependence of the C IV blueshift on QSO properties.

Some scenarios have been proposed to explain the physical origin of the C IV blueshift, and one of them is the orientation effect (Denney 2012). However, the scenario was excluded by Runnoe et al. (2014), who found no correlation between the C IV blueshift and the orientation based on a sample of radio core dominance. On the other hand, the large $L_{\mathrm{Bol}}/L_{\mathrm{Edd}}$ can cause high-blueshift emission lines, as mentioned above. In general, the QSOs with high $L_{\mathrm{Bol}}/L_{\mathrm{Edd}}$ display more apparent blueshift before approaching saturated luminosity. It indicates that the radiation pressure plays an important role in driving the shift of the peak wavelength of emission lines.

With the principal component analysis (PCA) of the low-z PG sample, Boroson & Green (1992) found that principal component 1 (PC1) is related to the relative strength of optical Fe II to Hβ (R_{Fe}, the ratio between the strength of Fe II emission and Hβ) and that principal component 2 (PC2) links optical luminosity and α_{ox}. With Hβ-based M_{BH}, Boroson (2002) suggested that PC1 is mainly correlated with $L_{\mathrm{Bol}}/L_{\mathrm{Edd}}$ and PC2 has a strong connection with M_{BH} and $L_{\mathrm{Bol}}/L_{\mathrm{Edd}}$. We explore the relationship between the C IV blueshift, PC1/PC2, and R_{Fe} for PG QSOs. It is found that the C IV blueshift has a very weak correlation with PC1 or R_{Fe}, but has a medium-strength correlation with PC2. The correlation coefficients are −0.11, 0.15, and −0.33 for PC1, R_{Fe}, and PC2, respectively. The relation between PC1/PC2 and $L_{\mathrm{Bol}}/L_{\mathrm{Edd}}/M_{\mathrm{BH}}$ needs to be investigated with more reliable measurements of M_{BH} in QSOs.

In order to explore the relationship between EW (C IV) and the C IV blueshift, We choose a subsample containing 67 PG QSOs and 43 high-z QSOs from our sample. These high-z QSOs have C IV emission line S/N $>$ 5 and $z > 2$. Figure 7 shows the relationship between EW (C IV) and the C IV blueshift. A medium-strength correlation is found between them ($r = -0.41$), which is consistent with the wind–disk model of BLRs given by Richards et al. (2011). Higher $L_{\mathrm{Bol}}/L_{\mathrm{Edd}}$ may lead to the formation of a wind component. If the BLR is dominated by the wind component, broad emission lines will show the blueshift and their strength will be suppressed (Richards et al. 2011).

Alternatively, Shemmer & Lieber (2015) pointed out that the lowest scatter relationship is not continuum versus EW (C IV), but rather Hβ-based $L_{\mathrm{Bol}}/L_{\mathrm{Edd}}$, i.e., the modified Baldwin effect (MBE). The MBE can also be used to explain the relationship between the total EW (C IV) and the C IV blueshift. As $L_{\mathrm{Bol}}/L_{\mathrm{Edd}}$ changes, there are expected changes in the thickness of the inner accretion disk, which may well affect the ionization of the BLR and a disk wind. However, weak-line QSOs deviating considerably from the classical Baldwin effect and MBE in Shemmer & Lieber (2015) reveal that the relationship between the profile and EW (C IV) may not only depend on $L_{\mathrm{Bol}}/L_{\mathrm{Edd}}$, but also additional physical properties (such as BLR geometry, density, and metallicity). Furthermore, if objects are viewed pole-on, then these objects will exhibit a narrower line width (Shen & Ho 2014), but actually lower $L_{\mathrm{Bol}}/L_{\mathrm{Edd}}$. The orientation effect will result in a larger deviation from MBE for weak-line QSOs. Broadly speaking, the orientation effect cannot be the main explanation of the EW change. In addition, we find that some objects with high $L_{\mathrm{Bol}}/L_{\mathrm{Edd}}$ deviate from the relationship between $L_{\mathrm{Bol}}/L_{\mathrm{Edd}}$ and blueshift (Figure 6), suggesting that these objects might suffer from the orientation bias.

The relationship between EW (C IV) and the C IV blueshift also supports the classical Baldwin effect originating from the softening of high-energy photons (Netzer et al. 1992; Korista et al. 1998; Dietrich et al. 2002). As suggested by Richards et al. (2011), the reduction of the number of high-energy photons that can ionize gas is beneficial to the formation of the wind component, thus enhancing the blueshift and reducing the EW. The wind component is not separated from the disk component in our fitting model. Therefore we are not sure that whether the Baldwin effect is triggered by the disappearance or weakness of the wind component.

3.2. C IV-based M_{BH} Correction with the C IV Blueshift

It is found that the C IV-based M_{BH} is biased with respect to that based on Hβ (Bian et al. 2012; Shen & Liu 2012). This bias is suggested to be corrected by the C IV blueshift (Coatman et al. 2017; Jun et al. 2017). Figure 8 shows the relationship between the M_{BH} difference (C IV-based M_{BH} and Hβ-based M_{BH}) and the C IV blueshift. It is found that there is a medium-strong correlation between them with the correlation coefficient of $r = 0.35$ and the probability of the null hypothesis of $p = 2.2 \times 10^{-4}$. The black line is the best fit of the BCES bisector. The formula is

$$\log(M_{\mathrm{BH}}(\mathrm{C\,IV}/\mathrm{H}\beta)) = -0.34(\pm 0.09) + 6.31(\pm 1.57) \times 10^{-4}\, V(\mathrm{C\,IV}). \quad (4)$$

The red and green dashed lines in Figure 8 are from Jun et al. (2017) and Coatman et al. (2017), respectively. We correct the C IV-based M_{BH} according our best fit and find that the mean

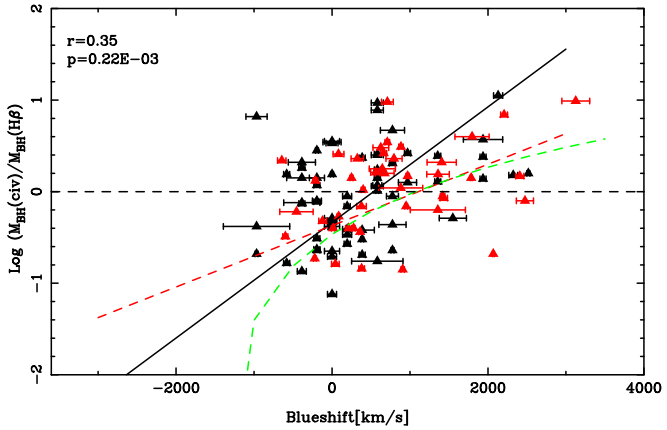

Figure 8. Effect of the C IV velocity shift on the difference between M_{BH} based on C IV and Hβ. The black solid line is the best fit of the BCES bisector. Red and green dashed lines are the relations from Jun et al. (2017) and Coatman et al. (2017). The correlation coefficients are listed at the top of the panel. The objects used for the analysis are the same as those in Figure 7.

value and the dispersion of the M_{BH} difference are 0.012 and 0.48 dex, respectively, which shows that some other parameters are need to be considered in the calculation of M_{BH} from the C IV line.

Compared to Hβ-based M_{BH}, many previous studies have shown that the C IV-based single-epoch SMBH mass usually exhibits significant scatter (Baskin & Laor 2004b; Richards et al. 2011; Bian et al. 2012; Denney 2012; Shen & Liu 2012). Coatman et al. (2017) used a high-z AGN sample ($1.5 < z < 4.0$) to investigate the relationship between the C IV blueshift and C IV-based M_{BH}. They found that C IV-based M_{BH} may be a factor 5 to 10 larger than Balmer-line-based M_{BH} at the C IV blueshift of more than 3000 km s^{-1} and gave an empirical correction for the C IV-based M_{BH} based on the relation between the C IV blueshift and the ratio of C IV FWHM to Hα FWHM. In contrast, Mejía-Restrepo et al. (2018) used a larger sample (including the objects from Coatman et al. 2017) and showed that the relation between FWHM (C IV/Hα)/FWHM (C IV/Mg II) and the C IV blueshift is driven by the relation between the C IV blueshift and C IV FWHM, which suggested that the empirical correction constructed by the C IV blueshift and Balmer-line width for C IV-based single-epoch M_{BH}, therefore, the L_{Bol}/L_{Edd}, is limited. In addition, they also found that there is no connection between Mg II and C IV profiles according to the PCA analysis, suggesting that high-ionization (C IV) and low-ionization (Hα, Mg II) lines are distinct.

We find the C IV blueshift is indeed related to the ratio of M_{BH} (Figure 8). However, our correction for C IV-based single-epoch M_{BH} is limited considering the large system error of M_{BH}, which also seems to support the conclusion given by Mejía-Restrepo et al. (2018) that solely using the C IV line width may not get the reliable virialized M_{BH}. Line peak ratios need to be considered (Runnoe et al. 2013; Brotherton et al. 2015). To understand how to improve the accuracy of C IV-based single-epoch M_{BH}, large samples including low- and high-z AGNs are required for future analysis.

The difference of the results among Coatman et al. (2017), Mejía-Restrepo et al. (2018), and our work may originate from the sample selection. The similarity about the samples is that all of these studies use the sample of Shen & Liu (2012). However, most of the objects in Shen & Liu (2012) are $z < 1.7$, which leads the incompleteness of the C IV profiles in the blue waveband. Therefore, the profile parameters, such as FWHM and EW may be inaccurate for these objects. We select objects with $z > 2.0$ to avoid the issue and investigate the effects of the C IV blueshift on C IV-based single-epoch M_{BH} in Section 3.2. In addition, a difference in the samples is the utilization of PG QSOs ($z < 0.5$) in this work. PG QSOs have lower bolometric luminosity than high-z QSOs ($z > 2.0$), which allow us to expand our results to the end of low luminosity.

4. Conclusion

For a collected sample of low-z and high-z QSOs, spectral decomposition is used to investigate the blueshift of C IV broad emission line relative to systemic, which is defined by [O III] λ5007. The results are as follows.

(1) It is confirmed that a blueshift exists for the high-ionization C IV broad emission line in the rest frame defined by the narrow [O III] line or Hβ. It is found that there is a medium-strong positive correlation between the C IV blueshift and the luminosity of continuum or L_{Bol}/L_{Edd}, and a medium negative relationship between the C IV blueshift and EW(C IV). These results are consistent with the picture that radiation pressure is correlative to the C IV blueshift.

(2) There is a medium-strong correlation between the ratio of C IV-based M_{BH} to Hβ-based M_{BH} and the C IV blueshift. This relationship depends on the accurate systemic redshift and the Hβ-based M_{BH}. A larger sample is needed to investigate this relationship.

We would like to thank M. S. Brotherton for the useful discussions. This work is supported by the National Key Research and Development Program of China (No. 2017YFA0402703). This work has been supported by the National Science Foundations of China (Nos. 11373024, 11233003, and 11873032).

Appendix

ORCID iDs

Xue Ge https://orcid.org/0000-0002-8348-2783
Bi-Xuan Zhao https://orcid.org/0000-0002-5413-3680
Wei-Hao Bian https://orcid.org/0000-0002-2121-8960

References

Abazajian, K. N., Adelman-McCarthy, J. K., Agüeros, M. A., et al. 2009, ApJS, 182, 543
Anand, M. Y., Kagali, B. A., & Murthy, J. 2009, BASI, 37, 1
Assef, R. J., Denney, K. D., Kochanek, C. S., et al. 2011, ApJ, 742, 93
Baskin, A., & Laor, A. 2004a, MNRAS, 350, L31
Baskin, A., & Laor, A. 2004b, MNRAS, 356, 1029
Bian, W.-H., Fang, L.-L., Huang, K.-L., & Wang, J. M. 2012, MNRAS, 427, 2881
Bian, W.-H., He, Z.-C., Green, R., et al. 2016, MNRAS, 456, 4081
Boroson, A. T., & Green, R. F. 1992, ApJS, 80, 109
Boroson, T. A. 2002, ApJ, 565, 78
Brandt, W. N., Laor, A., & Wills, B. J. 2000, ApJ, 528, 637
Brotherton, M. S., Runnoe, J. C., Shang, Z., & DiPompeo, M. A. 2015, MNRAS, 451, 1290

Brotherton, M. S., Wills, B. J., Steidel, C. C., & Sargent, W. L. W. 1994, ApJ, 423, 131
Cardelli, J. A., Clayton, G. C., & Mathis, J. S. 1989, ApJ, 345, 24
Coatman, L., Hewett, P. C., Banerji, M., & Richards, G. T. 2017, MNRAS, 465, 2120
Collin, S., Kawaguchi, T., Peterson, B. M., & Vestergaard, M. 2006, A&A, 456, 75
Denney, K. D. 2012, ApJ, 759, 44
Dietrich, M., Hamann, F., Shields, J. C., et al. 2002, ApJ, 581, 912
Du, P., Zhang, Z. X., Wang, K., et al. 2018, ApJ, 856, 6
Gaskell, C. M. 1982, ApJ, 263, 79
Ge, X., Bian, W.-H., Jiang, X.-L., Liu, W.-S., & Wang, X.-F. 2016, MNRAS, 462, 966
Gunn, J. E., Siegmund, W. A., Mannery, E. J., et al. 2006, AJ, 131, 2332
Hewett, P. C., & Wild, V. 2010, MNRAS, 405, 2302
Kaspi, S., Smith, P. S., Netzer, H., et al. 2000, ApJ, 533, 631
Jun, H. D., Im, M., Kim, D., & Stern, D. 2017, ApJ, 838, 41
Jun, H. D., Im, M., Lee, H. M., et al. 2015, ApJ, 806, 109
Korista, K., Baldwin, J., & Ferland, G. 1998, ApJ, 507, 24
Laor, A., & Brandt, W. N. 2002, ApJ, 569, 641
Leighly, K. M. 2004, ApJ, 611, 125
Marconi, A., Risaliti, G., Gilli, R., et al. 2004, MNRAS, 351, 169
Marziani, P., Sulentic, J. W., Dultzin-Hacyan, D., Calvani, M., & Moles, M. 1996, ApJS, 104, 37
McLure, R. J., & Jarvis, M. J. 2002, MNRAS, 337, 109
Mejía-Restrepo, J. E., Trakhtenbrot, B., Lira, P., & Netzer, H. 2018, MNRAS, 478, 1929
Murray, N., Chiang, J., Grossman, S. A., & Voit, G. M. 1995, ApJ, 451, 498
Netzer, H., Laor, A., & Gondhalekar, P. M. 1992, MNRAS, 254, 15
Netzer, H., Lira, P., Trakhtenbrot, B., Shemmer, O., & Cury, I. 2007, ApJ, 671, 1256
Onken, C. A., & Kollmeier, J. A. 2008, ApJ, 689, L13
Pâris, I., Petitjean, P., Ross, N. P., et al. 2016, A&A, 597, A79
Proga, D., Stone, J. M., & Kallman, T. R. 2000, ApJ, 543, 686
Richards, G. T., Kruczek, N. E., Gallagher, S. C., et al. 2011, AJ, 141, 167
Richards, G. T., Vanden Berk, D. E., Reichard, T. A., et al. 2002, AJ, 124, 1
Runnoe, J. C., Brotherton, M. S., DiPompeo, M. A., & Shang, Z. 2014, MNRAS, 438, 3263
Runnoe, J. C., Brotherton, M. S., Shang, Z., & DiPompeo, M. A. 2013, MNRAS, 434, 848
Schmidt, M., & Green, R. F. 1983, ApJ, 269, 352
Shemmer, O., & Lieber, S. 2015, ApJ, 805, 124
Shemmer, O., Netzer, H., Maiolino, R., et al. 2004, ApJ, 614, 547
Shen, Y., Brandt, W. N., Richards, G. T., et al. 2016, ApJ, 831, 7
Shen, Y., & Ho, L. C. 2014, Natur, 513, 210
Shen, Y., & Liu, X. 2012, ApJ, 753, 125
Shen, Y., Richards, G. T., Strauss, M. A., et al. 2011, ApJS, 194, 45
Shi, Y., Rieke, G. H., Ogle, P. M., et al. 2014, ApJS, 214, 23
Sulentic, J. W., Marziani, P., & Dultzin-Hacyan, D. 2000, ARA&A, 38, 521
Sun, M. Y., Xue, Y. Q., Richards, G. T., et al. 2018, ApJ, 854, 128
Tytler, D., & Fan, X. M. 1992, ApJS, 79, 1
Vanden Berk, D. E., Richards, G. T., Bauer, A., et al. 2001, AJ, 122, 549
Vestergaard, M., & Peterson, B. M. 2006, ApJ, 641, 689
Wang, H. Y., Wang, T., Zhou, H., et al. 2011, ApJ, 738, 85
Wang, J. M., Du, P., Brotherton, M. S., et al. 2017, NatAs, 1, 775
Wang, J. M., Qiu, J., Du, P., & Ho, L. C. 2014, ApJ, 797, 65
Wang, J. M., & Zhou, Y. Y. 1999, ApJ, 516, 420
Wills, B. J., Brotherton, M. S., Fang, D., Steidel, C. C., & Sargent, W. L. W. 1993, ApJ, 415, 563
Wu, J., Vanden Berk, D. E., Brandt, W. N., et al. 2009, ApJ, 702, 767
York, D. G., Adelman, J., Anderson, J. E., Jr., et al. 2000, AJ, 120, 1579